Comparison of the mechanical performance of architected three-dimensional intertwined lattices at the macro/microscale

Zacharias Vangelatos, Chenyang Li, Costas Grigoropoulos, Kyriakos Komvopoulos [*]

Department of Mechanical Engineering, University of California, Berkeley, CA 94720, USA

ARTICLE INFO

ABSTRACT

The design of lattice structures with exceptional mechanical performance has been accentuated by recent advances in both additive manufacturing and mechanical modeling. Although there is a plethora of different lattice structures with intriguing properties, such as auxeticity and reciprocity, an exceptional class of lattice geometries is that of intertwined lattices, designed by the tactical coalition of polyhedral structures. Although the superior mechanical performance of the latter structures has been demonstrated at the microscale, their mechanical analysis is still incipient. In this study, the design principles and mechanical performance of such three-dimensional structures were examined at the macroscale and juxtaposed with their microscale counterparts. As a proof of concept, the first stellation of the rhombic dodecahedron, an ultralight/ultrastiff architected structure with superior stiffness and strain hardening characteristics, was examined both numerically and experimentally. Finite element analysis showed that intertwining greatly enhances both the stiffness and isotropic behavior of the structure. In addition, mechanical testing of both microscale and macroscale structures revealed that lattice intertwining leads to commensurate stiffness and strain energy density compared to that of the bulk material, even for 20% relative density. The findings of this study pave the way for a systematic and rigorous approach to design and modeling of macroscopic intertwined geometries, for comparing them with their microscopic equivalents, and for providing insight into scale effects on the mechanical performance of architected materials with intertwined lattices.

© 2020 Elsevier Ltd. All rights reserved.

1. Introduction

The numerous intriguing properties of architected materials have motivated many studies in additive manufacturing and fundamental mechanics [1]. There are various categories of architected geometries, such as plate structures [2] and origami inspired designs [3,4], that have been thoroughly investigated. Plate structures have been found to exhibit isotropic behavior and stiffness approaching the theoretical Hashin–Shtrikman upper bound [2]. Although origami structures also consist of plate elements, their geometry and mechanical properties are reconfigurable since they are simply supported at their edges. Moreover, recent advances in structural design have inspired the use of origami structures to control wave propagation [5].

Another important category of tailored geometries is that of lattice structures. Because these structures comprise beam members that can be easily fabricated at various length scales and their mechanical behavior has been systematically studied [1,6],

they have been used in several engineering disciplines. A characteristic example is energy absorbing materials [7,8] that can sustain large recoverable deformation under both static [9] and dynamic loads [10]. In addition, several designs encompassing auxeticity [11–15], large energy absorption [16], and sensing capabilities [17] have been proposed. Designs including quasi-random porous materials [11], star-shaped formations [14], and hierarchical materials [13] have been employed to design biomaterials, such as artificial bone [6]. Additionally, biomimetic foam structures have been used in regenerative tissue engineering to construct implants with desirable mechanical properties [18].

Imitating polycrystalline designs at the macroscale has been accomplished by exploiting the same hardening and strengthening mechanisms observed at the microscale, leading to the design of non-monolithic lattice structures [19]. The concept of reconfiguration from the perspective of mechanical performance has also been explored for lattice structures [4]. Most notably, programmable active lattices that alter their behavior from stretching to bending dominated and vice versa have enabled the fabrication of ultrastiff, high-energy absorption materials [20]. Structure reconfiguration may also be instigated by the deformation of the structure. These design concepts combined with recent advances in three-dimensional (3D) printing of highly stretchable

---

* Corresponding author.
 E-mail addresses: cgrigoro@berkeley.edu (C. Grigoropoulos),
kyriakos@me.berkeley.edu (K. Komvopoulos).

materials [21] can forge programmable malleability depending on the loading conditions [22]. Major progress regarding the enhancement of the isotropic behavior of lattice structures has also been reported in recent studies [23,24]. Isotropy is imperative to the design of conventional engineering structures with properties independent of the loading direction. While tacit instantiations and improvements have been encountered, future progress can make lattice structures comparable to isotropic plate structures through the development of more rigorous mechanical design methodologies [2]. Although controlling scale effects in macroscopic bodies consisting of microscopic unit cells is possible, this is a major design challenge because it requires microscale printing techniques that can print on large surface areas. These types of effects have been studied with pentamode metamaterials exhibiting nonuniform material distribution of their beam members that can be easily fabricated even with conventional 3D printing techniques [25–27]. Nevertheless, they have not been investigated in more complex lattice structures consisting of uniform unit cells that are also fabricated by such printing techniques.

All of these remarkable properties are a consequence of tailoring the buckling response of the lattice structure [28]. Because buckling is a mechanism of structural instability, it is necessary to consider both the geometry of the structure and the applied load [29]. Tailored buckling can affect lattice densification, consequently increasing the stiffness and resilience to large deformations of the structure [30,31]. In addition, controlled buckling can be used as a bistability mechanism to tune the equilibrium positions and enhance the energy absorption capacity of the structure [32]. While buckling mechanisms manifest themselves differently at the length scale of a unit cell and that of an array, e.g., short- versus long-wavelength buckling [33], it is necessary to investigate whether these effects commence before fracture causes catastrophic collapse of the structure.

In previous investigations, buckling was controlled by the orderly post-contact behavior of lattice members and the assembly of the lattice unit cells. This approach led to the design of intertwined structures demonstrating high densification of their hyper unit cells, propelled by the interpenetration of neighboring polyhedral structures [34,35]. Specifically, it was proven that the intersection of proximal lattice members densifies the unit cell, enhances the stiffness of even bending dominated structures, and yields unprecedented strain hardening behavior under cyclic loading. However, all of these attributes are greatly affected by the material performance under loading conditions conducive to excessive deformation, where buckling contributes to plastic deformation and post contact of the lattice members [36]. While the materials used at the microscale embosom this intrinsic mechanical performance, the polymeric materials used in conventional large-scale 3D printing are fairly brittle, exhibiting limited or no plastic behavior [37,38]. Therefore, it is questionable whether these structures can also be effectively used at the macroscale for structural engineering applications.

The objective of this study was to investigate and compare the mechanical performance of macroscopic and microscopic intertwined lattice structures. In particular, a main goal was to examine the scalability of unit cells from the perspectives of 3D printing and mechanical behavior. Using the first stellation (FS) of the rhombic dodecahedron [34] as the baseline unit cell, it was investigated whether controlled interpenetration of neighboring unit cells can also enhance the mechanical performance at the macroscale. For a valid evaluation, the FS structure was compared to one of the most thoroughly investigated lattice structures, that is, the octet truss (OT), and its respective bulk material. Finite element analysis (FEA) provided insight into the effects of unit cell interpenetration, resulting in densification and affecting the directional stiffness and material isotropy. Mechanical testing of

structures fabricated by 3D printing and multiphoton lithography (MPL) at the macroscale and microscale, respectively, and FEA simulations were used to evaluate the mechanical properties of aforementioned 3D lattice structures relative to those of their bulk material. To provide insight into scale effects on the mechanical performance of architected structures with intertwined lattices, the mechanical performance of the 3D printed macrostructures are compared with that of the MPL fabricated microstructures.

2. Mechanical characterization

Fig. 1 shows the design and relative density of the FS and OT macrostructures examined in this study. The OT architected geometry [1,7,21] is shown in Fig. 1A. The intertwined geometry used in this study was inspired by the FS of the rhombic dodecahedron. The FS unit cell of the structure consists of three octahedra — two octahedra are rotated by 90° in the clockwise and counterclockwise directions with respect to the central axis of the stationary third octahedron (Fig. 1B). To augment lattice intertwining, each of the stellated geometries was connected edge-to-edge with neighboring unit cells, resulting in the formation of a structure with interpenetrating proximal unit cells. A thorough analysis of the conceptual process used to design such geometries has been reported elsewhere [34]. Because lattice intertwining utilizes the internal vacant space of the unit cells, it can enhance densification significantly. In contrast to the OT unit cell, which does not have any fastigiated beam members on its faces, such as the beam members extending outwardly from the faces of the FS unit cell as pyramidal protrusions (Fig. 1B), the beams of the hyper unit cell formed by the assembly of 9 (i.e., 3×3 array) FS unit cells produce a conglomeration of beams in the interior of the lattice structure (Fig. 1C). Hereafter, this structure will be referred to as the FS hyper unit cell. The relative densities of both structures are compared in Fig. 1D. By measuring the volume of each structure from the CAD files using the ANSYS 18.0 Design Modeler and then curve fitting the obtained data, the following equations of the relative density $\bar{\rho}$ of the FS and OT macroscopic structures were obtained

$$\bar{\rho}_{\text{FS}} = 139.4 \left(\frac{r}{L}\right)^2 - 7.678 \left(\frac{r}{L}\right)^3 \tag{1}$$

and

$$\bar{\rho}_{\text{OT}} = 71.38 \left(\frac{r}{L}\right)^2 - 4.099 \left(\frac{r}{L}\right)^3, \tag{2}$$

where r and L are the radius and the length of the lattice beam members, respectively. Eqs. (1) and (2) indicate that the relative density is a cubic polynomial of r/L, which includes the effect of the volume of the joints of the structure on the relative density that becomes significant for $\bar{\rho} > 0.05$. The good fit of Eqs. (1) and (2) to corresponding CAD data, evidenced from Fig. 1D, indicates that the two-term polynomial functions can accurately describe the variation of the relative density in the r/L range of this study. Although there are other intertwined geometries that demonstrate significantly higher densification, such as the three-compound octahedron [35], the spatial orientation of the regular polyhedra of such structures reduces the gaps at their faces, making the removal of supporting material in macroscale 3D printing considerably more challenging. The same challenge can be encountered with microstructures fabricated with the MPL process because overlapping of sections of the structure may contain unpolymerized material that cannot be dissolved during fabrication [34]. However, the orientation of the three octahedra in the FS unit cell offsets this design constraint, as seen in Fig. 1C.
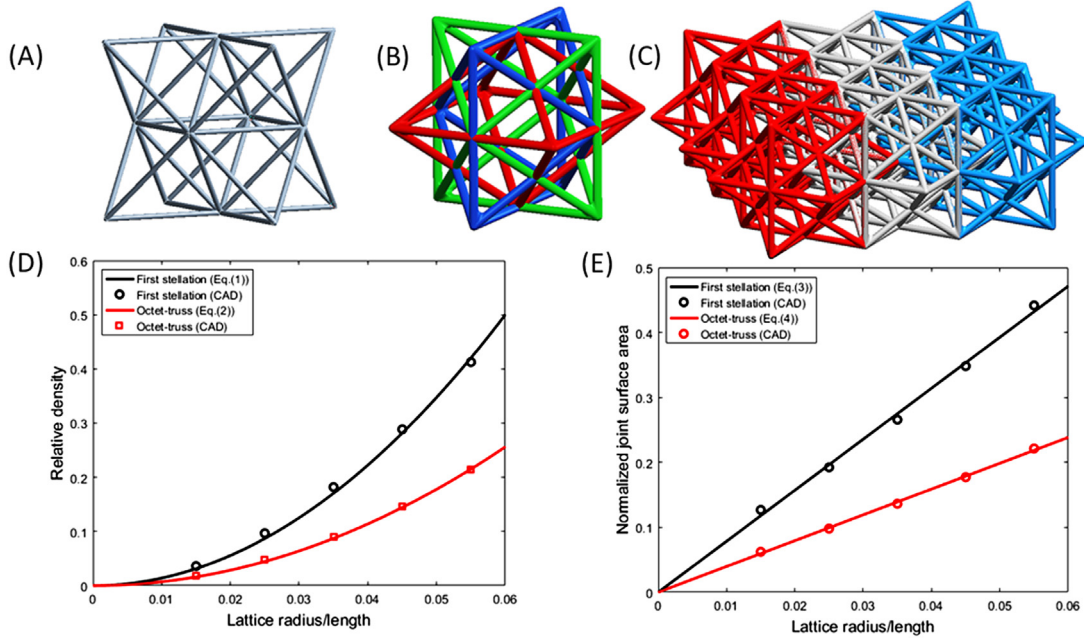
Fig. 1. Design and relative density of the octet truss (OT) and first stellation (FS) macrostructures. Side views of the (A) OT unit cell, (B) FS unit cell consisting of three octahedra that were offset by 90° from each other, and (C) FS hyper unit cell constructed by merging three FS unit cells distinguished by different colors. (D) Relative density versus lattice radius/length ratio. (E) Normalized joint surface area versus lattice radius/length ratio. The intertwined lattice members of the FS macrostructure enhance more the relative density and the joint surface area compared to the OT macrostructure.. (For interpretation of the references to color in this figure legend, the reader is referred to the web version of this article.)

A comparison of the connectivity and length distribution of the beam members in the two designs was made by considering the number of beams connected at the joints of each structure. The length of all the OT beam members is equal to $L/\sqrt{2}$, whereas the length of half of the FS beam members is equal to $\sqrt{3}L/2$ and that of the other half is equal to $L/2$. It will be shown later that this length distribution in the network of each structure affects the spatial stress distribution significantly. From the total number of beam joints in the OT structure, 57% are 3-beam joints, while the rest are 8-beam joints. The beam joints in the FS structure comprise 44.4% 4-beam joints, 44.4% 6-beam joints, and 11.2% 8-beam joints. Therefore, the joint contribution to the structure rigidity differs significantly in the two designs. The difference in joint rigidity can be further quantified by comparing the joint surface area A_j to the total surface area of the structure A_s (determined from the CAD files) as a function of r/L. This was accomplished by computing the difference between A_s and the surface area of all the beam members A_b (not including A_j) and defining the normalized joint surface area by $\bar{A} = A_j/A_s$, where $A_j = A_b - A_s$. Fig. 1E shows CAD data of $\bar{A}$ for different r/L values and best-fit curves for the FS and OT structures, with equations given by

$$\bar{A}_{\text{FS}} = 7.854 \left(\frac{r}{L}\right) \tag{3}$$

and

$$\bar{A}_{\text{OT}} = 3.972 \left(\frac{r}{L}\right) \tag{4}$$

Eqs. (3) and (4) indicate that the joint surface area in the FS structure is larger than that in the OT structure by a factor of ∼2. The significant difference in joint surface area of the two structures has a significant effect on the overall enhancement of the structural stiffness.

The average coordination number was used to determine whether the mechanical response of the structures was bending or stretching dominated. The calculated coordination number of the FS hyper unit cell was found to be equal to 8, classifying it as a bending dominated structure [39]. This implies that the stiffness of the FS structure should be significantly lower than that of the stretching dominated OT structure. However, FEA simulations of the directional stiffness of each structure revealed that the densification caused by the lattice intertwining compensated for this effect. Because the OT structure exhibits cubic symmetry, its elastic behavior can be fully characterized by three elastic constants (C_{11}, C_{12}, and C_{44}), whereas the elastic behavior of the FS structure that demonstrates tetragonal symmetry is governed by six elastic constants (C_{11}, C_{12}, C_{13}, C_{44}, and C_{66}). (The indices of the elastic constants are based on the Voigt notation of the stiffness tensor.) To calculate the elastic constants, FEA simulations were performed with the ANSYS Workbench 18.0 code, using a numerical technique that provides close matching between theoretical and experimental results of anisotropic structures [23]. Both structures were meshed with 10-node tetrahedral elements. The OT unit cell consisted of 21974 elements and 9963 nodes, whereas the FS hyper unit cell consisted of 76513 elements and 35902 nodes. To ensure elastic deformation, both structures were subjected to very small strains ($<10^{-5}$). As discussed in the next section, the experimentally determined elastic modulus of the bulk material used in 3D printing is equal to 160 MPa. Since this material exhibits behavior close to incompressible, its Poison's ratio was set equal to 0.499. Because the desired direction of stiffness enhancement is perpendicular to the top face of the OT unit cell and the FS hyper unit cell (Figs. 1A and 1C), this study was focussed on augmenting the mechanical performance of the structure in the [001] direction. The stiffness of the OT unit cell and the FS hyper unit cell in this direction was calculated from the following equations (Voigt notation):

$$E_{[001]_{\text{OT}}} = \frac{C_{11}(C_{11} + C_{12}) - 2C_{12}^2}{C_{11} + C_{12}} \tag{5}$$

and

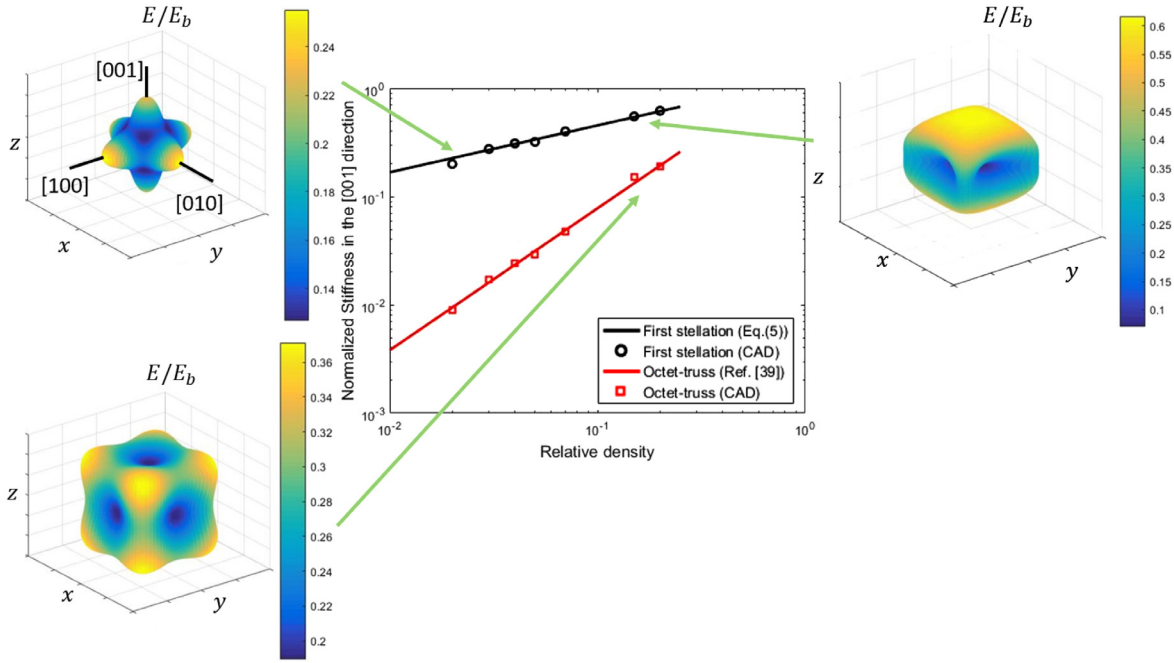$$E_{[001]_{\text{FS}}} = \frac{C_{33}(C_{11} + C_{12}) - 2C_{13}^2}{C_{11} + C_{12}}. \tag{6}$$

Fig. 2. Numerical results of the normalized stiffness E/E_b of the first stellation (FS) and the octet truss (OT) macrostructures. Despite the fact that the FS is a bending dominated structure, its normalized stiffness is significantly higher than that of the OT because of the significant number of beam members connected at the joints of the FS structure. In addition, although the shape of the 3D stiffness map of the OT macrostructure does not vary with the relative density [36], the intertwined beam members in the FS macrostructure change both the shape of its stiffness map and its anisotropic behavior.

Calculating the elastic constants for different relative densities yielded an Ashby chart of normalized stiffness $\bar{E} = E/E_b$, where E_b is the stiffness of the bulk material, of the FS hyper unit cell (Fig. 1D) and the OT unit cell (Fig. 1A), which is shown in Fig. 2. On the basis of this Ashby chart, it may be interpreted that the FS stiffness in the [001] direction is significantly higher than that of the OT, despite the fact that FS is a bending dominated structure. A best fit of the OT stiffness versus relative density data obtained from the FEA analysis yielded an equation similar to that reported elsewhere [39]. The normalized stiffness of the FS hyper unit cell, obtained by curve fitting the FEA data points shown in Fig. 2, is given by

$$\bar{E}_{[001]_{FS}} = 14.485 \bar{\rho}^{1.31}. \tag{7}$$

Furthermore, because of the significant effect of lattice intertwining on the anisotropy of the FS hyper unit cell at different relative densities, it is necessary to consider the directional stiffness at an arbitrary direction $\boldsymbol{n}$, given by

$$E(\boldsymbol{n}) = \frac{1}{(\boldsymbol{n} \otimes \boldsymbol{n}) : \boldsymbol{C}^{-1} (\boldsymbol{n} \otimes \boldsymbol{n})}, \tag{8}$$

where $\boldsymbol{C}^{-1}$ is the compliance tensor of the lattice structure. For structures lacking intertwined lattices, such as the OT, the size of the stiffness map increases with the relative density without changing its shape [37]. The stiffness map of the OT unit cell is the same with that obtained from analytical expressions reported elsewhere [40], providing validation to the FEA of this study. Alternatively, the shape of the FS stiffness map shows a dependence on relative density. Particularly, for $\bar{\rho}_{FS} = 0.02$, the stiffness map demonstrates a star-like shape, whereas for $\bar{\rho}_{FS} = 0.2$ the stiffness map is more uniform. The variation of the anisotropy of the FS hyper unit cell and the invariance of the anisotropy of the OT unit cell can be quantified in terms of the anisotropy Zenner ratio A [23], which for cubic symmetry is defined by

$$A_{OT} = \frac{2C_{44}}{C_{11} - C_{12}}. \tag{9}$$

When $A = 1$, the structure is said to exhibit isotropic behavior. However, Eq. (9) is only valid for structures demonstrating cubic symmetry. The variation of the stiffness map of the FS hyper unit cell indicates a changing anisotropy. The degree of anisotropy for different structural symmetries can be quantified by the magnitude of the universal elastic anisotropy index [41]. Because the FS hyper unit cell demonstrates tetragonal symmetry, its universal elastic anisotropy index A^u is given by [41]

$$A_{FS}^u = \langle \boldsymbol{C} \rangle : \langle \boldsymbol{S} \rangle - 6 \tag{10}$$

where $\langle \boldsymbol{C} \rangle$ is the average stiffness tensor and $\langle \boldsymbol{S} \rangle$ is the average compliance tensor. For an isotropic structure, $A^u = 0$. Each average tensor was obtained by calculating the average of each component using the transformation tensor

$$\boldsymbol{Q} = \begin{bmatrix} \cos\theta & \sin\theta & 0 \\ -\sin\theta & \cos\theta & 0 \\ 0 & 0 & 1 \end{bmatrix} \begin{bmatrix} 1 & 0 & 0 \\ 0 & \cos\varphi & \sin\varphi \\ 0 & -\sin\varphi & \cos\varphi \end{bmatrix}, \tag{11}$$

where φ and θ are polar and azimuthal angles, respectively. Using the summation rule, the average $\langle C_{ijkl} \rangle$ components of the $\boldsymbol{C}$ tensor were calculated from the following formula

$$\langle C_{ijkl} \rangle = \frac{1}{4\pi} \int_0^\pi \int_0^{2\pi} Q_{ip}Q_{jq}Q_{kr}Q_{ls}C_{pqrs} \sin\theta \, d\theta \, d\varphi, \tag{12}$$

where the indices range from 1 to 3. The $\sin\theta$ function is included in Eq. (12) because all directions are assumed to have a uniform distribution (i.e., probability density $= \sin\theta \, d\theta \, d\varphi / 4\pi$). Eq. (12) gives the average tensor component as the summation of the transformed tensor in every direction in the 3D space. Using Eq. (12) to calculate the components of the average tensors in Eq. (10) provides the universal elastic anisotropy index. To make the latter comparable to the anisotropy index for cubic symmetry (Zenner index), the following equation can be used [41]

$$A_{FS}^{eq} = \left(1 + \frac{5}{12}A_{FS}^u\right) + \sqrt{\left(1 + \frac{5}{12}A_{FS}^u\right)^2 - 1}. \tag{13}$$
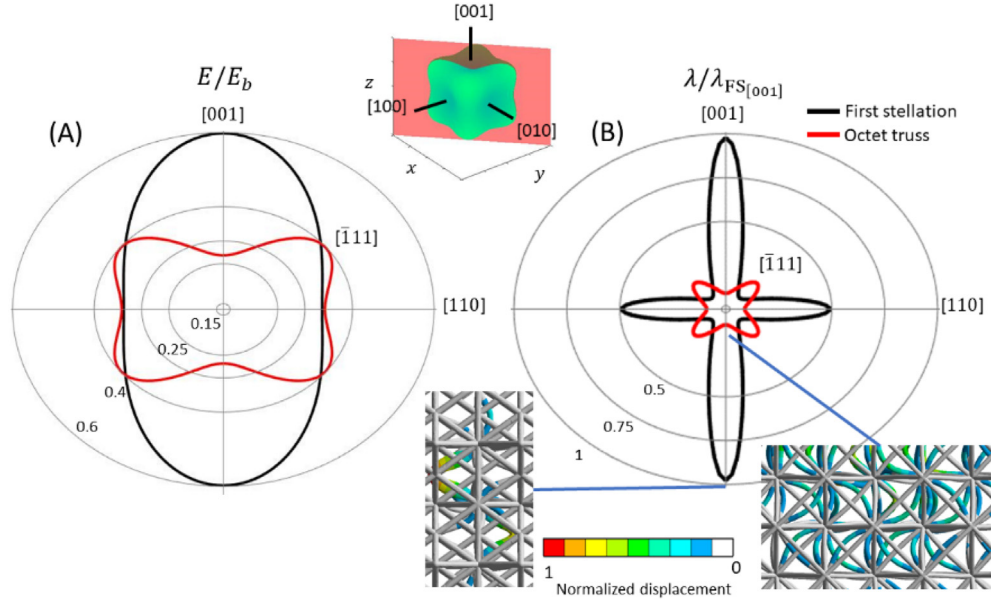
Fig. 3. Maps of (A) normalized directional stiffness E/E_b and (B) critical buckling load $\lambda/\lambda_{FS[001]}$ of the first stellation (FS) and octet truss (OT) macrostructures for fixed relative density ($\bar{\rho} = 0.02$) plotted on the (110) plane. The stiffness of the FS macrostructure is significantly higher than that of the OT macrostructure in the [001] direction. The intertwined unit cells at this specific alignment enhance the stiffness of the FS macrostructure between the $\pm 45°$ directions and the [001] direction. Although the desired direction of stiffness enhancement is the [001] direction, different spatial orientations of the intertwined unit cells may increase the stiffness in different orientations. The critical buckling load of the FS macrostructure is significantly higher than that of the OT macrostructure in all directions except in the domain defined by the $\pm 30°$ directions and the [$\bar{1}11$] direction, a consequence of the lower FS stiffness in these directions and the differences in the inertia of the structures in various directions. The buckling mode in the [001] direction is characterized by the twisting of beam members at the center of both structures, although beam buckling is significantly more pronounced in the OT structure.

While $A_{OT} = 6.35$ (i.e., independent of $\bar{\rho}_{OT}$), $A_{FS}^{eq} = 14.96$ and 8.54 for $\bar{\rho}_{FS} = 0.02$ and 0.2, respectively. This is indicative of the anisotropy variance in intertwined geometries with different relative densities, a characteristic not observed with unit cells that are not intertwined with neighboring unit cells [42]. The reason for the anisotropy variance is that an increase in beam radius leads to localized "bulk" spots in the unit cell. As the relative density increases, these spots begin to merge, creating a bulk core in the structure. This trend is apparent in non-intertwined geometries at very high relative densities. However, at a very high relative density the unit cell becomes like the bulk material and, consequently, its mechanical behavior is governed by the properties of the bulk material, not those of the architected design. Nevertheless, the FS hyper unit cell exhibits anisotropy variance at a much lower relative density (i.e., $\bar{\rho}_{FS} = 0.2$).

A more succinct comparison of the directional normalized stiffness E/E_b of the FS hyper unit cell and the OT unit cell for fixed relative density ($\bar{\rho}_{FS} = \bar{\rho}_{OT} = 0.02$) is shown in Fig. 3A. This figure was produced by projecting the directional stiffness map onto the (110) plane. It can be seen that despite the significant enhancement of the stiffness of the FS hyper unit cell (179% higher than that of the OT unit cell in the [001] direction), this effect is encountered between the $\pm 45°$ directions and the [001] direction. Nevertheless, in the vast majority of the literature, the OT structure has been tested in the [001] direction [1,7,21,38], presumably due to the high stress developing at the corners of the unit cell when loaded in the [111] direction, which coincides with the maximum stiffness of the structure.

A buckling analysis was also performed to determine the critical buckling load of the FS and OT structures in the [001] direction of the stiffness enhancement. Specifically, the instability of infinitely large structures consisting of periodic arrays of the FS and OT unit cells was examined by fixing one plane of the structure and applying a unit load to the mirror plane of the structure. The critical buckling load of each structure was obtained by solving the eigenvalue relation

$$\det \left[\mathbf{K}_m - \lambda \mathbf{K}_g (\boldsymbol{\sigma}) \right] = 0, \tag{14}$$

where λ is the critical buckling load, $\mathbf{K}_m$ is the linear elastic stiffness matrix, and $\mathbf{K}_g$ is the geometric stiffness matrix, which depends on the applied stresses $\boldsymbol{\sigma}$. Eq. (14) indicates that a structure instability occurs when the potential energy of the system reaches a local maximum. Further details about the derivation of Eq. (14) can be found elsewhere [29]. For consistency with the directional E/E_b map (Fig. 3A), the directional normalized critical buckling load $\lambda/\lambda_{FS[001]}$ was also mapped onto the (110) plane (Fig. 3B). The significantly higher critical buckling load in the [001] direction of the FS structure than that of the OT structure is attributed to the higher stiffness of the FS structure in that direction and the different directional dependence of the inertia matrix of each structure. It is noted that the OT structure displays a higher critical buckling load between the $\pm 30°$ directions and the [$\bar{1}11$] direction, in accord with the higher stiffness of the OT structure in this range (Fig. 3A). Interestingly, the buckling mode of both structures comprises twisting of internal beam members (normal displacement distributions are shown as insets in Fig. 3B). However, the significantly larger number of beam members in the OT structure undergoing buckling indicates a higher likelihood for the simultaneous collapse of more beam members compared to the FS structure.

3. Experiments

To validate the enhancement of the mechanical performance in the [001] direction owing to lattice intertwining, mechanical testing was performed with macrostructures fabricated by 3D printing using a Stratasys Objet260 Connex3 multi-material printer. The structural material was PolyJet VeroWhitePlus RGD835 photopolymer resin, whereas the soluble support material for 3D printing was PolyJet FullCure 706. After 3D fabrication, the support material was removed with a water jet. To validate
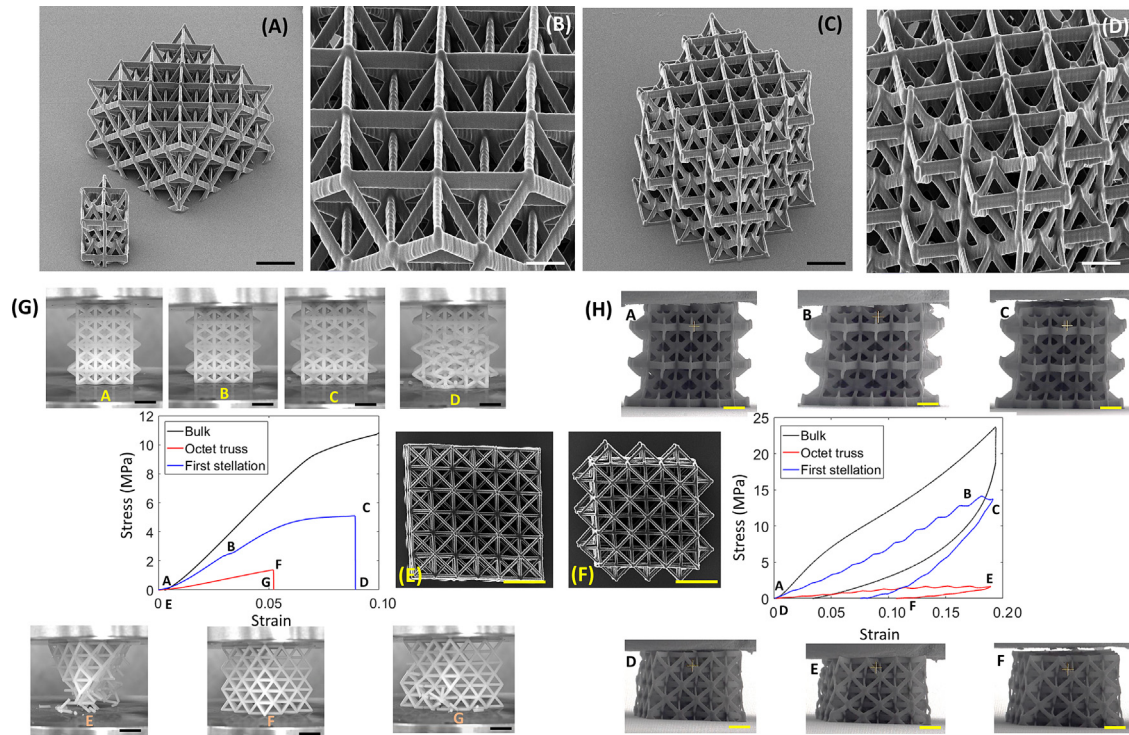
Fig. 4. (A–F) HIM images of microstructures fabricated by MPL and (G, H) representative stress–strain responses with SEM images of deformed structures obtained at characteristic loading stages. The stress–strain response of the respective bulk structure is also shown for comparison. (A) Isomeric view of the OT microstructure (scale bar = 5 µm). (B) Close-up view of the OT microstructure showing the uniform beam intersection at all joints of the structure (scale bar = 2 µm). (C) Isomeric view of the FS structure (scale bar = 5 µm). (D) Close-up view the FS microstructure showing more beams intersecting at the joints compared to the OT microstructure (scale bar = 2 µm). (E) Top view of the OT microstructure (scale bar = 10 µm). (F) Top view of the FS microstructure (scale bar = 10 µm). (G) The mechanical response of the FS and OT macrostructures. The FS macrostructure shows a transition from elastic deformation (AB range) to a stress plateau terminated by the instigation of buckling (point C) and the subsequent instantaneous collapse of the structure (point D). Alternatively, the OT macrostructure demonstrates a linear elastic behavior (EF range), exhibiting fracture at significantly lower stress and strain that activates the spontaneous collapse of the structure (point G) (scale bars = 10 mm). (H) The mechanical response of the FS and OT microstructures. The FS microstructure demonstrates an elastic response (AB range) until the instigation of buckling in some bottom beam members (point B), resulting in the drop of the stress–strain curve (BC range). Unloading reveals that buckling resulted in irreversible deformation. The OT microstructure also exhibits a linear elastic behavior (DE range) until the beam members that sustained large deformation as a result of bending begin to deform plastically (point F) (scale bars = 5 µm).

the mechanical properties of the bulk material, 30 × 30 × 30 mm blocks were also fabricated by 3D printing. The OT and FS macrostructures were fabricated to have a surface area of 30 × 30 mm² and a relative density of 0.2. At lower relative densities, the beam members were damaged and fractured during the removal of the support material. The FS macrostructure consisted of 1 × 1 × 3 hyper unit cells, each having 9 FS unit cells, whereas the OT macrostructure consisted of 3 × 3 × 3 unit cells. Mechanical tests were performed with an Instron-5500 apparatus, using a compression rate fixed at 2 mm/min. For statistical analysis, 5 macrostructures of each design were tested under identical conditions. All of the lattice macrostructures were tested up to the instigation of fracture. The experiments were recorded with a high-speed camera (i-SPEED 3, ix Cameras). Characteristic recordings of the tested OT and FS macrostructures can be seen in Videos A and B, respectively, of the Supplementary Information (SI).

Furthermore, to compare with the mechanical performance at the microscale, the same structure geometries were fabricated with the MPL process, a highly efficient process for fabricating complex 3D microstructures, using the photoresist ZS2080 as structural material. Details about the MPL apparatus and the preparation of the microstructures can be found elsewhere [34]. Fig. 4 shows characteristic helium ion microscopy (HIM) images of microstructures fabricated by MPL. An isomeric and a close-up view showing the joints of intersecting beam members of the OT microstructure are shown in Figs. 4A and 4B, respectively. Similarly, an isomeric view and a close-up view of the joints of significantly more intersecting beam members (analysed in section 2) of

the FS microstructure are shown in Figs. 4C and 4D, respectively. Figs. 4E and 4F show top views of the OT and FS microstructures where the loading was applied during mechanical testing. To examine the mechanical performance at the microscale, in situ compression tests were performed with a picoindenter (PI 85 SEM PicoIndenter, Hysitron) placed inside a scanning electron microscope (FEI Quanta 3D FEG). This setup enables high-precision nanomechanical testing and real-time recording of the deformation process. The compression tests were conducted with a flat cylindrical molybdenum tip (model #72SC-D3/035 (407AM)) with a diameter equal to 130 µm. The maximum tip displacement was set at 5 µm, whereas the deformation rate was fixed at 800 nm/s. While the macrostructures were tested up to fracture, the mechanical performance of the microstructures was evaluated only in the plastic deformation range because of the limited maximum force applied by the picoindenter. Characteristic recordings of the tested FS and OT microstructures can be seen in Videos C and D of the SI, respectively.

4. Results and discussion

Fig. 4 shows representative stress–strain responses of the macroscopic and microscopic FS and OT structures and respective bulk structures. The stress in the macroscale tests was calculated by dividing the load with the contact area of the rigid plate with the macrostructure, determined from the FEA contact simulations. This was accomplished by assigning 8-node surface elements to the beam members of the contacting surfaces of the

Table 1

Numerical and experimental results of the elastic stiffness and strain energy density of bulk, FS, and OT macroscopic and microscopic structures.

Structure	Mechanical properties					
	Numerical		Experimental			
	Elastic stiffness E (MPa)		Elastic stiffness E (MPa)		Strain energy density* u (kJ/m^3)	
	Macro	Micro	Macro	Micro	Macro[a]	Micro[b]
Bulk	160	95	160 ± 5.0	95.38 ± 3.22	76.02 ± 1.52	2285.3 ± 100.5
First stellation (FS)	89.8	68	86.5 ± 1.4	65.13 ± 5.81	28.12 ± 3.15	1324.0 ± 58.3
Octet truss (OT)	30.4	15	29.03 ± 0.08	16.69 ± 1.57	3.28 ± 0.83	196.4 ± 15.7

[a]For an objective comparison, the stain energy density of the bulk and FS macrostructures was obtained at a strain equal to the fracture strain (0.05) of the OT macrostructure.

[b]The strain energy density of all microstructures was computed at the maximum strain (0.19) achieved in these tests.

macrostructure and the plate. While at the instigation of deformation the contact area was very small, it increased with the applied load, eventually reaching a constant value of 738.63 mm^2 for the FS macrostructure and 1477.25 mm^2 for the OT macrostructure for a downward displacement of the rigid plate by 0.1 mm. These values of the contact area were used to compute the stress during the entire loading cycle of each macrostructure. In the MPL fabrication, the beam members were fabricated by scanning the laser beam multiple times over the same path, which resulted in the formation of small joint protrusions. While this suggested that contact of the tip would be confined at the joints of the beam members at the contact face of the microstructures, after a very small downward displacement of a few nm the tip came into contact with the cusps of the beam members as with the macroscopic structures. Therefore, considering the similarity in structure and contact area at both scales, the stress in the microscale experiments was calculated by dividing the load with the contact area computed in the macroscale experiments expressed in units of nm^2, i.e., contact area of 738.63 and 1477.254 nm^2 for the FS and OT microscale structures, respectively. The strain was obtained as the ratio of the vertical displacement of the rigid plate (or tip) to the height of the undeformed structure. The bulk material was compressed up to the available maximum force of the Instron machine or the picoindenter apparatus. A significantly greater capacity for ductile deformation was observed at the microscale. While the OT and FS macrostructures fractured at a strain of 0.05 and 0.09, respectively, both the OT and FS microstructures exhibited plastic deformation without fracturing up to a strain of 0.19. This result reveals a different effect of the structure geometry on the mechanical behavior at each scale. Because the FS structure demonstrated a brittle-like behavior at the macroscale, the mechanical behavior was controlled by the initial configuration of the lattice members. At the microscale, however, when the FS microstructure experienced post-yield deformation, contact of the beam members that sustained large deformation inhibited fracture, resulting in ductile-like behavior. While this was one of the principal design objectives of the intertwined lattice structures, as per previous reports [34], the present study shows that the design principle of post-contact behavior is redundant at the macroscale. Therefore, the elastic analysis presented in the previous section is cogent at the macroscale.

The differences in the mechanical behavior of the structures at the two length scales can be further interpreted in terms of their respective stiffness, strain energy density, and critical buckling load. The elastic stiffness E and strain energy density u of each structure at both length scales are given in Table 1. The stiffness was measured as the slope of the stress–strain curve at the beginning of loading, whereas the strain energy density was obtained as the area under the stress–strain curve at a fixed strain. To compare the mechanical performance of the FS macrostructure with that of its respective bulk structure and the OT macrostructure, the corresponding strain energy densities were calculated for a strain equal to 0.05, which is the fracture

strain of the OT macrostructure (Fig. 4A). As mentioned in the previous section, the mean value of the measured bulk stiffness (160 MPa) was used in all the FEA simulations. Because the microstructures did not fracture, their strain energy density was computed for a strain equal to 0.19 (Fig. 4B) corresponding to the maximum load applied to the microscale structures.

A comparison of the stress–strain responses shown in Fig. 4 and the data given in Table 1 reveals a superior mechanical performance of the FS structure compared to the OT structure at both scales. Specifically, the FS macrostructure demonstrated a monotonically increasing stress–strain response, reaching a stress plateau before the instigation of fracture (point C in Fig. 4A). However, the OT macrostructure exhibited a linear stress–strain response and failed at a much lower stress and strain (point F in Fig. 4A) compared to the FS macrostructure. This result indicates a significantly higher (by a factor of ~5.4) strain energy density at fracture for the FS structure than the OT structure at the macroscale. Moreover, at a strain equal to 0.05, the FS macrostructure demonstrated a strain energy density equal to ~37% of its bulk material (Table 1), showing that the FS macrostructure can absorb a high amount of strain energy despite having 80% less material than the respective bulk structure. In addition, the FS macrostructure showed ~8.6 times higher strain energy density (at a strain of 0.05) compared to the OT macrostructure (Table 1). This finding is important for ultralight structure applications that can potentially utilize beam structures, such as those used in aerospace engineering [43]. In addition, as shown in Table 1, the stiffness of the FS macrostructure is ~3 times higher than the OT stiffness and ~54% of the bulk stiffness. Importantly, even though the FS macrostructure possesses a bending dominated geometry, it is about three times stiffer than the OT macrostructure, which is a stretching dominated structure, a finding consistent with the FEA simulation results.

Moreover, it is instructive to examine the stress distribution in both macrostructures and juxtapose the origin of failure with that observed in the macroscale experiments. Figs. 5A and 5B show von Mises equivalent stress distributions in the FS and OT macrostructures, respectively, obtained from a linear elastic FEA. While the stress is uniformly distributed across the OT beam members (Fig. 5B), only the vertical beam members of the FS macrostructure sustained high stress, while the stress in the rest of the beams is almost zero (Fig. 5A). This result is in agreement with the failure mechanisms observed at both length scales, where failure was found to commence in the vertical beam members. In addition, the results shown in Figs. 5A and 5B explain why the FS macrostructure maintained its structural integrity, with only a small number of beam members exhibiting failure. The uniform stress distribution in all of the unit cells of the OT macrostructure is also consistent with the failure of this structure at both length scales, where a group of unit cells failed simultaneously as opposed to only a few beam members failing in the FS structure. This is further evidence of the superior
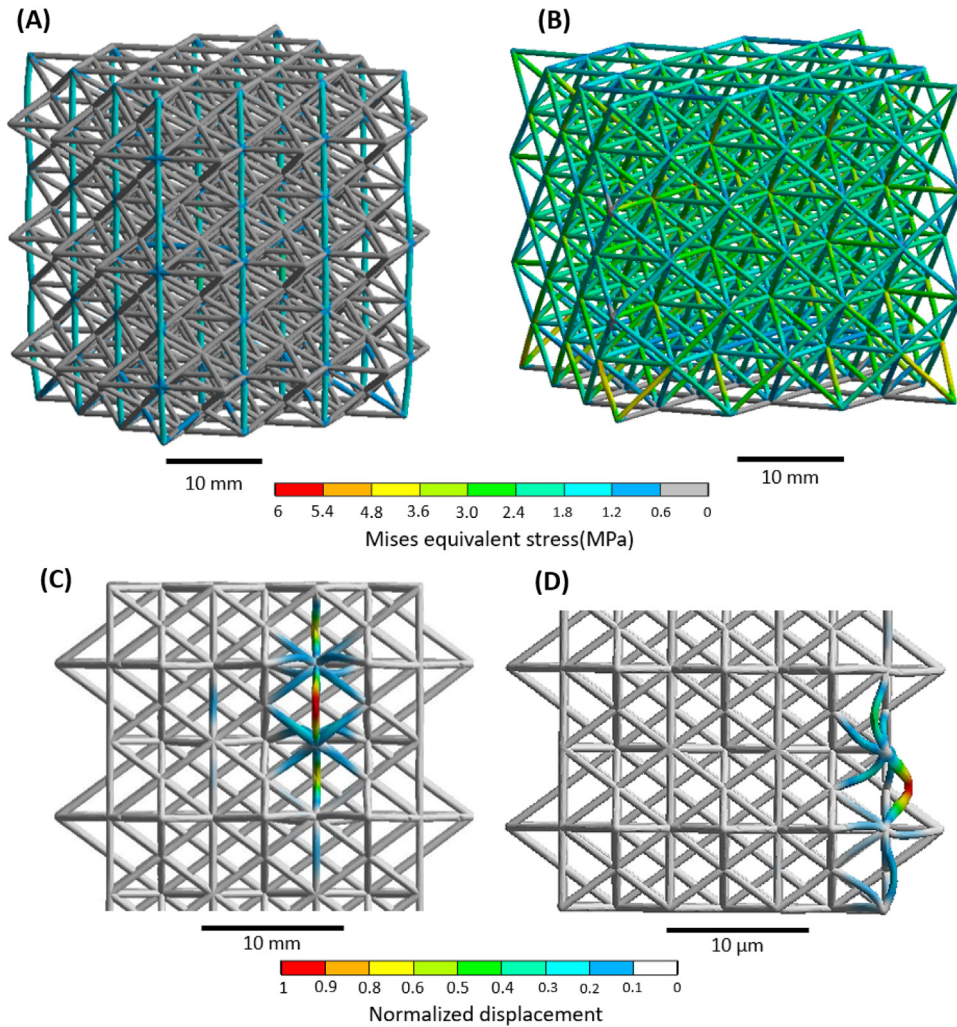
Fig. 5. Distribution of the von Mises equivalent stress in the (A) FS and (B) OT macrostructures revealing the development of high stresses only in the vertical beams of the FS macrostructure, with the rest of the beams showing almost zero stress, and a uniform distribution of higher stress in the beams of all the unit cells of the OT macrostructure. Eigenvalue buckling mode of the FS hyper unit cell for loading applied to (C) the cusps of top beam members of the FS macrostructure and (D) the joints of top beam members of the FS microstructure. In the former case, the first mode encompasses twisting of a joint at the top of the hyper unit cell, presumed to be responsible for the subsequent fracture of the FS macrostructure observed in the macroscale experiments, whereas in the latter case, the first mode shows excessive beam bending at the bottom of the microstructure, consistent with the FS microstructure behavior observed in the microscale experiments.

mechanical behavior of the FS structure compared to the OT structure.

At the microscale (Fig. 4B), the FS structure demonstrated an increasing stress response up to a strain of 0.19, at which instant some beam members at the bottom of the microstructure buckled. The larger stress–strain hysteresis area of the FS microstructure compared to that of the OT microstructure reveals a significantly higher strain energy density for this microstructure. More specifically, the strain energy density of the FS microstructure is ∼6.7 times higher than that of the OT microstructure and ∼58% that of the bulk structure (Table 1). Likewise with the macroscale, the FS structure demonstrates significant strain energy capacity at the microscale. In addition, its elastic stiffness is ∼4.5 times higher than that of the OT microstructure and ∼71% of the respective bulk structure (Table 1). These results indicate that the FS structure exhibits a superior mechanical performance than the OT structure at both length scales, while it reserves a significant portion of the mechanical capacity of the bulk material, despite having only 20% of the volume of the bulk structure.

The critical buckling load and buckling modes of the FS structure were also examined at both length scales. The critical buckling load was computed by solving Eq. (14). The loading area used

in the eigenvalue buckling analysis matched that in the experiments. To apply the initial loading conditions in the experiments in the buckling analysis of the macrostructures, the load was applied at the cusps of the top beams that initially came into contact with the rigid plate, whereas in the buckling analysis of the microstructures, the load was applied to the joints of the top beam members. At both scales, the bottom nodes of the structures were fixed to prevent any movement during loading.

The critical buckling load of the FS macrostructure ($1 \times 1 \times 3$ hyper unit cells) was found to be equal to 3706.4 N, which is in close agreement with the experimentally measured buckling load of 3735 ± 30 N. In addition, a close inspection of the deformation response shown in Video B of the SI shows localized twisting of the beam members at the top of the FS macrostructure before the instigation of fracture. This failure mode is the same as the buckling eigenvector mode obtained from the FEA simulations (Fig. 5C). However, the critical buckling load of the OT macrostructure ($3 \times 3 \times 3$ unit cells) was found to be equal to 6926.4 N, which is ∼1.87 times that of the FS macrostructure, implying premature failure of the OT macrostructure before buckling, which for a material demonstrating limited plasticity, such as the resin material used to fabricate the macrostructures,

will lead to brittle fracture. The foregoing scenario is validated by the absence of any buckling events during testing of the OT macrostructure, as seen in Video A of the SI. Another potential reason for the premature failure of the OT macrostructure is that the FS hyper unit cells have disproportionally more beam members connected to their joints compared to the OT unit cells, implying a greater enhancement of the FS structural integrity. Specifically, while there are 4 beams projecting outwardly from each face of the FS unit cell (Fig. 1B), such beams do not exist in the OT unit cell (Fig. 1A). This is because non-intertwined geometries, such as the OT, are not augmented with this critical feature. Hence, the OT is negatively affected by higher stress concentration effects leading to premature collapse.

The critical buckling load of the FS microstructure was found to be equal to 10.3 mN, which is close to the experimental value of 10.27 $\pm$ 0.055 mN. As seen in Video C of the SI, the buckling instability in the FS microstructure commenced at the end of loading upon the collapse of bottom beam members. This deformation mode is consistent with the eigenvalue buckling mode (Fig. 5D) for the respective loading conditions. However, the critical buckling load of the OT microstructure was found to be equal to 18.73 mN, which is ∼1.82 times that of the FS microstructure. Although the deformation of the OT microstructure, seen in Video D of the SI, demonstrated excessively large deformation of some beam members, the absence of a discernible abrupt drop in the respective stress–strain response (Fig. 4B) suggests that these beam members bent but did not buckle. Therefore, plastic deformation developed in the OT microstructure at a much lower load than the critical buckling load. It should be noted that the critical buckling load of the infinitely large structure consisting of FS hyper unit cells was found to be higher than that of the infinitely large structure consisting of OT unit cells, evidently because of the different sizes of the structures and boundary conditions used in the two buckling analyses.

Although all of the above results illuminate the superior mechanical performance of the FS structure relative to the OT structure and its light weight efficiency compared to the bulk structure at both length scales, it is informative to place these results in perspective with each other and with previously reported results [34–36]. One of the principal characteristics of lattice intertwining is that large deformation causes the beam members to come into contact, consequently enhancing the stiffness and strain energy density of the structure in a manner mimicking strain hardening. This effect occurs during plastic deformation, when the beams sustain very large strains. As a result, FS microlattices demonstrate an order of magnitude higher strain hardening than the bulk material [34]. The obtained results elucidate the specific mechanical attributes of intertwined structures at different length scales. Because the fabrication material of the microscopic lattices exhibits significant ductility, these structures demonstrated high energy dissipation in plastic deformation mode. Hence, geometric effects of lattice intertwining become more important from the perspective of tactical densification and post contact. Alternatively, the fairly rigid structural material used to fabricate the macroscopic lattices necessitates architecting the structures such that to enhance their mechanical behavior in the elastic deformation mode. Therefore, the initial configuration of the lattice structure is critical at the macroscale. This is important consideration for optimizing the design strategy depends on the length scale and intertwining geometry.

The present analysis shows that intertwined structures are characterized by high stiffness and high strain energy density at both microscale and macroscale, using either brittle or ductile materials for their fabrication. In addition, the intriguing concept of variable anisotropy [23] enables the relative density to be used as a design parameter to control the directional stiffness of the structure. However, this was accomplished by merging different unit cells [23], not by intertwining select beam members. Therefore, different orientations of intertwined geometries must be explored to obtain lattice structures demonstrating isotropic behavior at low relative densities. Although this may increase the complexity of the design, optimization techniques, such as machine learning, can be used to identify such structures for a wide range of orientations [44]. Additionally, tailoring the directional stiffness may lead to novel dynamic behaviors, such as tailored bandgaps in dispersion curves of resonant metamaterials for controlling wave propagation [45]. The foregoing effects observed with intertwined structures provide impetus for developing new design strategies for metamaterials with architected lattices demonstrating unprecedented mechanical performance.

5. Conclusions

Experimental and numerical studies were undertaken to investigate the mechanical behavior of macroscopic and microscopic structures possessing intertwined lattices fabricated by 3D printing and MPL, respectively. FEA simulations showed that the elastic stiffness can be tailored and enhanced even for a bending dominated structure and that the anisotropic behavior of the structure can be altered by intertwining the lattice members. Mechanical testing of the FS structure revealed both high stiffness and strain energy density despite having only 20% of the volume of the respective bulk structure. The obtained results indicate that the superior stiffness and strain energy density of intertwined geometries can be realized either under purely elastic deformation conditions at the macroscale or in the presence of excessive plasticity at the microscale. This study paves the way for the investigation and utility of intertwined structures for controlling the anisotropy of ultralight/ultrastiff geometries at micro/macroscales, which is of particular importance in large-scale engineering applications and microstructural engineering of structures. In addition, it promulgates how different mechanical effects manifest themselves at different length scales, depending on the fabrication material and deformation regime.

Declaration of competing interest

The authors declare that they have no known competing financial interests or personal relationships that could have appeared to influence the work reported in this paper.

Appendix A. Supplementary data

Supplementary material related to this article can be found online at https://doi.org/10.1016/j.eml.2020.100930.

References

[1] A.A. Zadpoor, Mechanical meta-materials, Mater. Horiz. 3 (2016) 371–381.

[2] Y. Wang, O. Sigmund, Quasiperiodic mechanical metamaterials with extreme isotropic stiffness, Extreme Mech. Lett. 34 (2020) 100596.

[3] A.L. Wickeler, H.E. Naguib, Novel origami-inspired metamaterials: Design, mechanical testing and finite element modelling, Mater. Des. 186 (2020) 108242.

[4] H. Fang, S.-C.A. Chu, Y. Xia, K.-W. Wang, Programmable self-locking origami mechanical metamaterials, Adv. Mater. 30 (2018) 1706311.

[5] H. Yasuda, Y. Miyazawa, E.G. Charalampidis, C. Chong, P.G. Kevrekidis, J. Yang, Origami-based impact mitigation via rarefaction solitary wave creation, Sci. Adv. 5 (2019) eaau2835.

[6] W. Wu, W. Hu, G. Qian, H. Liao, X. Xu, F. Berto, Mechanical design and multifunctional applications of chiral mechanical metamaterials: A review, Mater. Des. 180 (2019) 107950.

[7] M. Mohsenizadeh, F. Gasbarri, M. Munther, A. Beheshti, K. Davami, Additively-manufactured lightweight metamaterials for energy absorption, Mater. Des. 139 (2018) 521–530.

[8] P. Vuyk, S. Cui, R.L. Harne, Illuminating origins of impact energy dissipation in mechanical metamaterials, Adv. Eng. Mater. 20 (2018) 1700828.

[9] S. Yuan, C.K. Chua, K. Zhou, 3D-printed mechanical metamaterials with high energy absorption, Adv. Mater. Technol. 4 (2019) 1800419.

[10] X. An, C. Lai, W. He, H. Fan, Three-dimensional meta-truss lattice composite structures with vibration isolation performance, Extreme Mech. Lett. 33 (2019) 100577.

[11] J.N. Grima, L. Mizzi, K.M. Azzopardi, R. Gatt, Auxetic perforated mechanical metamaterials with randomly oriented cuts, Adv. Mater. 28 (2016) 385–389.

[12] Y. Qin, X. Li, Y. Chen, M. Lu, Tunable auxetic mechanical metamaterials with "arch-shaped" units, Phys. Status Solidi 13 (2019) 1800376.

[13] R. Gatt, L. Mizzi, J.I. Azzopardi, K.M. Azzopardi, D. Attard, A. Casha, J. Briffa, J.N. Grima, Hierarchical auxetic mechanical metamaterials, Sci. Rep. 5 (2015) 8395.

[14] L. Mizzi, E.M. Mahdi, K. Titov, R. Gatt, D. Attard, K.E. Evans, J.N. Grima, J.-C. Tan, Mechanical metamaterials with star-shaped pores exhibiting negative and zero Poisson's ratio, Mater. Des. 146 (2018) 28–37.

[15] H. Yang, L. Ma, Multi-stable mechanical metamaterials with shape-reconfiguration and zero Poisson's ratio, Mater. Des. 152 (2018) 181–190.

[16] S. Cui, B. Gong, Q. Ding, Y. Sun, F. Ren, X. Liu, Q. Yan, H. Yang, X. Wang, B. Song, Mechanical metamaterials foams with tunable negative Poisson's ratio for enhanced energy absorption and damage resistance, Materials 11 (2018) 1869.

[17] Y. Jiang, Z. Liu, N. Matsuhisa, D. Qi, W.R. Leow, H. Yang, J. Yu, G. Chen, Y. Liu, C. Wan, Z. Liu, X. Chen, Auxetic mechanical metamaterials to enhance sensitivity of stretchable strain sensors, Adv. Mater. 30 (2018) 1706589.

[18] F.S L. Bobbert, S. Janbaz, A.A. Zadpoor, Towards deployable meta-implants, J. Mater. Chem. B 6 (2018) 3449–3455.

[19] M.-S. Pham, C. Liu, I. Todd, J. Lertthanasarn, Damage-tolerant architected materials inspired by crystal microstructure, Nature 565 (2019) 305–311.

[20] M.A. Wagner, T.S. Lumpe, T. Chen, K. Shea, Programmable, active lattice structures: Unifying stretch-dominated and bending-dominated topologies, Extreme Mech. Lett. 29 (2019) 100461.

[21] Y. Jiang, Q. Wang, Highly-stretchable 3D-architected mechanical metamaterials, Sci. Rep. 6 (2016) 34147.

[22] Y. Wang, J.P. Groen, O. Sigmund, Simple optimal lattice structures for arbitrary loadings, Extreme Mech. Lett. 29 (2019) 100447.

[23] S. Xu, J. Shen, S. Zhou, X. Huang, Y.M. Xie, Design of lattice structures with controlled anisotropy, Mater. Des. 93 (2016) 443–447.

[24] T. Tancogne-Dejean, D. Mohr, Elastically-isotropic elementary cubic lattices composed of tailored hollow beams, Extreme Mech. Lett. 22 (2018) 13–18.

[25] A. Amendola, C.J. Smith, R. Goodall, F. Auricchio, L. Feo, G. Benzoni, F. Fraternali, Experimental response of additively manufactured metallic pentamode materials confined between stiffening plates, Compos. Struct. 142 (2016) 254–262.

[26] A. Amendola, G. Carpentieri, L. Feo, F. Fraternali, Bending dominated response of layered mechanical metamaterials alternating pentamode lattices and confinement plates, Compos. Struct. 157 (2016) 71–77.

[27] F. Fraternali, A. Amendola, Mechanical modeling of innovative metamaterials alternating pentamode lattices and confinement plates, J. Mech. Phys. Solids 99 (2017) 259–271.

[28] G. Oliveri, J.T.B. Overvelde, Inverse design of mechanical metamaterials that undergo buckling, Adv. Funct. Mater. 30 (2020) 1909033.

[29] S. Krenk, Non-Linear Modeling and Analysis of Solids and Structures, first ed., Cambridge University Press, Cambridge, UK, 2009, pp. 20–26.

[30] A. Rafsanjani, A. Akbarzadeh, D. Pasini, Snapping mechanical metamaterials under tension, Adv. Mater. 27 (2015) 5931–5935.

[31] Y. He, Y. Zhou, Z. Liu, K.M. Liew, Buckling and pattern transformation of modified periodic lattice structures, Extreme Mech. Lett. 22 (2018) 112–121.

[32] J. Hua, H. Lei, C.-F. Gao, X. Guo, D. Fang, Parameters analysis and optimization of a typical multistable mechanical metamaterial, Extreme Mech. Lett. 35 (2020) 100640.

[33] B. Haghpanah, J. Papadopoulos, D. Mousanezhad, H. Nayeb-Hashemi, A. Vaziri, Buckling of regular, chiral and hierarchical honeycombs under a general macroscopic stress state, Proc. R. Soc. Lond. Ser. A Math. Phys. Eng. Sci. 470 (2014) 20130856.

[34] Z. Vangelatos, V. Melissinaki, M. Farsari, K. Komvopoulos, C. Grigoropoulos, Intertwined microlattices greatly enhance the performance of mechanical metamaterials, Math. Mech. Solids 24 (2019) 2636–2648.

[35] Z. Vangelatos, K. Komvopoulos, J. Spanos, M. Farsari, C. Grigoropoulos, Anisotropic and curved lattice members enhance the structural integrity and mechanical performance of architected metamaterials, Int. J. Solids Struct. 193–194 (2020) 287–301.

[36] Z. Vangelatos, G.X. Gu, C.P. Grigoropoulos, Architected metamaterials with tailored 3D buckling mechanisms at the microscale, Extreme Mech. Lett. 33 (2019) 100580.

[37] M.E. Yildizdag, C.A. Tran, M. Spagnuolo, E. Barchiesi, F. dell'Isola, F. Hild, A multi-disciplinary approach for mechanical metamaterial synthesis: A hierarchical modular multiscale cellular structure paradigm, in: H. Altenbach, A. Öchsner (Eds.), in: State of the Art and Future Trends in Material Modeling, vol. 100, Springer, Switzerland, 2019, pp. 485–505.

[38] M.E. Yildizdag, E. Barchiesi, F. dell'Isola, Three-point bending test of pantographic blocks: Numerical and experimental investigation, Math. Mech. Solids (2020) http://dx.doi.org/10.1177/1081286520916911.

[39] L.R. Meza, G.P. Phlipot, C.M. Portela, A. Maggi, L.C. Montemayor, A. Comella, D.M. Kochmann, J.R. Greer, Reexamining the mechanical property space of three-dimensional lattice architectures, Acta Mater. 140 (2017) 424–432.

[40] M. Abdelhamid, A. Czekanski, Impact of the lattice angle on the effective properties of the octet-truss lattice structure, J. Eng. Mater. Technol. 140 (2018) 041010.

[41] S.I. Ranganathan, M. Ostoja-Starzewski, Universal elastic anisotropy index, Phys. Rev. Lett. 101 (2008) 055504.

[42] C.P. de Jonge, H.M.A. Kolken, A.A. Zadpoor, Non-auxetic mechanical metamaterials, Materials 12 (2019) 635.

[43] N.B. Cramer, D.W. Cellucci, O.B. Formoso, C.E. Gregg, B.E. Jenett, J.H. Kim, M. Lendraitis, S.S. Swei, G.T. Trinh, K.V. Trinh, K.C. Cheung, Elastic shape morphing of ultralight structures by programmable assembly, Smart Mater. Struct. 28 (2019) 055006.

[44] L. Wu, L. Liu, Y. Wang, Z. Zhai, H. Zhuang, D. Krishnaraju, Q. Wang, H. Jiang, A machine learning-based method to design modular metamaterials, Extreme Mech. Lett. 36 (2020) 100657.

[45] L. Van Belle, C. Claeys, E. Deckers, W. Desmet, On the impact of damping on the dispersion curves of a locally resonant metamaterial: Modelling and experimental validation, J. Sound Vib. 409 (2017) 1–23.